
CONVOLUTIONAL NEURAL GENERATIVE CODING: SCALING PREDICTIVE CODING TO NATURAL IMAGES

Alexander Ororbia
 Rochester Institute of Technology
 ago@cs.rit.edu

Ankur Mali
 University of South Florida
 ankurarjunmali@usf.edu

ABSTRACT

In this work, we develop *convolutional neural generative coding* (Conv-NGC), a generalization of predictive coding to the case of convolution/deconvolution-based computation. Specifically, we concretely implement a flexible neurobiologically-motivated algorithm that progressively refines latent state maps in order to dynamically form a more accurate internal representation/reconstruction model of natural images. The performance of the resulting sensory processing system is evaluated on several benchmark datasets such as Color-MNIST, CIFAR-10, and Street House View Numbers (SVHN). We study the effectiveness of our brain-inspired neural system on the tasks of reconstruction and image denoising and find that it is competitive with convolutional auto-encoding systems trained by backpropagation of errors and notably outperforms them with respect to out-of-distribution reconstruction (including on the full 90k CINIC-10 test set).

Keywords Predictive coding · Brain-inspired learning · Computer vision

1 Introduction

The algorithm known as backpropagation of errors [50] (or backprop) has served as a crucial element behind the tremendous progress that has been made in recent machine learning research, progress which has been accelerated by advances made in computational hardware as well as the increasing availability of vast quantities of data. Nevertheless, despite reaching or surpassing human-level performance on many different tasks ranging from those in computer vision [17] to game-playing [55], the field still has a long way to go towards developing artificial general intelligence. In order to increase task-level performance, the size of deep networks has increased greatly over the years, up to hundreds of billions of synaptic parameters as seen in modern-day transformer networks [12]. However, this trend has started to raise concerns related to energy consumption and as to whether such large systems can attain the flexible, generalization ability of the human brain [5]. Furthermore, backprop itself imposes additional limitations beyond its long-argued biological implausibility [11], such as its dependence on a global error feedback pathway for determining each neuron’s individual contribution to a deep network’s overall performance [30], resulting in sequential backward, non-local updates that make parallelization difficult, which stands in strong contrast to how learning occurs in the brain [23, 43, 42]. The limitations imposed by the prohibitively large size of these systems as well as the constraints imposed by their workhorse training algorithm, backprop, has motivated the investigation and development of alternative methodology.

Some of the most promising pathways come from the emerging domain of research known as brain-inspired computation, which seeks to develop neural architectures and their respective credit assignment algorithms that leverage only local information, motivated strongly by how learning is conducted by the brain. The promise of brain-inspired computing brings with it synaptic adjustment mechanisms that are neurobiologically-grounded [18] as well as neural computation and inference that is flexible, capable of conducting a wide variety of operations [37] at biologically more faithful levels [29, 36], facilitating massive algorithmic parallelization (at scale) and adaption on analog and neuromorphic hardware [14, 49, 24].

In addressing the many-fold challenges facing backprop-based ANNs and in the direction of brain-inspired computing, we design a new model for image processing, convolutional neural generative coding (Conv-NGC), which is inspired by human learning. It is well-known that humans process information with hierarchical top-down feed-forward and bottom-up backward connections, which continuously *predict and correct* humans’ internal

representations of that information [47]. In neuroscience, this interplay is known as predictive coding [47, 45]. Similarly, our Conv-NGC model also includes state prediction and correction steps that continuously generate and refine its internal representations (Figure 2). Furthermore, Conv-NGC encodes complex visual information by incorporating blocks of (de)convolutional into a top-down directed generative model within the computational framework of neural predictive coding [3, 8, 10, 39, 37].

Our contributions are as follows: **1)** We propose a new computer vision model, Conv-NGC, which acquires robust representations of natural images in an unsupervised fashion, **2)** To the best of our knowledge, this is the first work in the literature where visual inputs are processed using deep (de)convolutional layers directly and naturally within of computational framework of predictive coding, significantly enhancing its representation power for vision-based tasks, and, **3)** We demonstrate, on several natural color image datasets, that the proposed Conv-NGC is competitive with existing backprop-based neural models (of similar architectural designs) on the tasks of image reconstruction and image denoising and outperforms them with respect to out-of-distribution predictive modeling.

2 Convolutional Neural Generative Coding

We start by describing our model instantiation of convolutional neural generative coding (Conv-NGC), which is ultimately tasked from learning from streams of natural image data in an unsupervised fashion. Typically, in a visual recognition task, input data patterns belonging to different object classes, arranged into batches, are presented to a processing system at different time points for training. In this section, we describe our problem setup and our model architecture.

2.1 Problem Setup

With respect to the problem setup, a Conv-NGC system is tasked with processing a finite collection of images depicting a certain set of object classes arranged in an arbitrary order. The dataset contains a set of n input samples: $\mathcal{D} = \{(\mathbf{x}_1, \mathbf{y}_1) \dots (\mathbf{x}_n, \mathbf{y}_n)\}$. Here, $\mathbf{x}_j \in \mathcal{R}^{I \times I \times C}$ represents the image of the j^{th} input sample ($I \times I$ is the 2D shape of any single image channel and C is the number of channels, i.e., $C = 3$ for the red-green-blue channels) and $\mathbf{y}_j \in \{0, 1\}^{Y \times 1}$ is its ground truth class label (Y is the number of classes). Note that while we formalize the available labels in each benchmark dataset, the models that we develop and experiment with in this work are unsupervised and, as a result, never make use of the labels in \mathcal{D} .

Notation: In this study, we use the symbol \ast_s to refer to a strided convolution where s is the stride argument (note that \ast_1 means convolution with stride of 1, which would also be the same as just \ast). In contrast, the symbol \odot_s denotes deconvolution (or transposed convolution) with a stride of s . The hadamard product is denoted by \odot while \cdot represents a matrix/vector multiplication. $()^T$ denotes the transpose operation. Flatten(\mathbf{z}) means that the input tensor \mathbf{z} is converted to a column vector with a number of rows equal to the number of elements that it originally contained while UnFlatten(\mathbf{z}) is its inverse (i.e., it converts the vector back to its original tensor shape). Finally, Dilate(\mathbf{v}, s) is used to represent a dilation function controlled by the dilation (integer) size (e.g., $s = 2$). Further note that Conv-NGC is technically made up of 4D synaptic tensors and when we write \mathbf{W}_{ij} , we are saying that we are retrieving a 2D matrix at position (i, j) in the 4D tensor \mathbf{W} (if one wanted to obtain a specific scalar in \mathbf{W} , one would write W_{ijkl} without bold font).

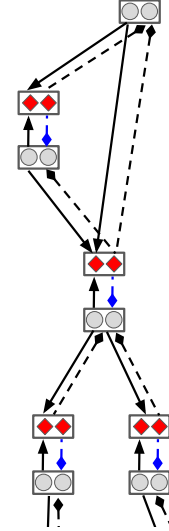


Figure 1: Depicted is a portion of an arbitrary NGC circuit. Grey circles are state units (deep excitatory pyramidal cells) and red diamonds are error units (superficial pyramidal cells). Solid arrows represent predictive pathways and dashed diamond pathways represent error transmission pathways.

2.2 Deep Convolutional Neural Coding

Our Conv-NGC is a generalization of the NGC computational predictive coding framework in [37] to the case of natural image data. The underlying process of Conv-NGC can be divided into three key components: **1)** local

prediction and error unit map calculation, **2)** latent state map correction, and **3)** local synaptic adjustment. See Figure 1 for a general depiction of an NGC circuit (and Figure 2 for a visual depiction of a Conv-NGC model).

The Neural Coding Process: Fundamentally, Conv-NGC consists of a set of L predictive layers (typically arranged hierarchically, though this is not a strict architectural requirement, e.g., Figure 1 depicts a non-hierarchical NGC circuit) that are designed to learn latent representations of observed patterns. It is important to note that, unlike the bottom-up forward propagation of a standard convolutional neural network (CNN), neural layers within a Conv-NGC system make top-down predictions, the errors of which are then used to subsequently correct the layers’ own values. In effect, this means that the layers in Conv-NGC are stateful and their computation within a forward pass can be further broken down into two distinct computations – top-down prediction and state correction.

First, in the top-down prediction phase, given its current state \mathbf{z}^ℓ (which abstractly models the functionality of deep excitatory pyramidal cells), each layer ℓ of our model tries to predict the state of the layer below it, yielding prediction $\bar{\mathbf{z}}^{\ell-1}$. At the bottom-most layer, the model predicts $\bar{\mathbf{z}}_x^0$ for the input data pattern (\mathbf{x}). Following this, a set of error neurons (which abstractly model the functionality of superficial pyramidal cells) compute the mismatch between this prediction and the actual state $\mathbf{z}^{\ell-1}$, i.e., $\mathbf{e}^{\ell-1} = (\mathbf{z}^{\ell-1} - \bar{\mathbf{z}}^{\ell-1})$.

Second, in the correction phase, the model’s internal state layers are corrected based on how accurate their top-down guesses turned out to be. The error/mismatch signal $\mathbf{e}^{\ell-1}$ computed during the prediction phase is subsequently used to adjust the current values of the state \mathbf{z}^ℓ that originally made the prediction $\bar{\mathbf{z}}^{\ell-1}$. This *local error correction*, which is not present in traditional feedforward ANNs, helps to nudge the state \mathbf{z}^ℓ towards a configuration (i.e., set of values) that better predicts the layer below in the future and thus, ultimately, moves the layer towards a better representation/higher-level abstraction of the input. This correction is “local” in the sense that each layer’s update depends only on its own (top-down) errors, which are produced by comparing its own values with the predictions made by the layer above it, and those of the layer immediately below it, i.e., the comparison between a layer’s prediction of a nearby layer’s state and that layer’s actual current state values.

Given the description of the two general computations above, we may now describe how Conv-NGC processes data. Unlike a standard feedforward ANN, which predicts \mathbf{y}_j given \mathbf{x}_j (or, in the case of auto-encoding, the ANN attempts to reconstruct \mathbf{x}_j itself given \mathbf{x}_j as input) with a single forward pass, our model works in multiple steps. First, a Conv-NGC network predicts the value of $\mathbf{z}^0 = \mathbf{x}_j$ from \mathbf{z}^1 (which generates prediction $\bar{\mathbf{z}}^0$), \mathbf{z}^1 from \mathbf{z}^2 (which generates prediction $\bar{\mathbf{z}}^1$), etc. As each prediction is made, the corresponding set of error neurons compute the mismatch between the predicted value and its target state layer.¹ Next, the neural system then corrects the values of its states $\{\mathbf{z}^1, \mathbf{z}^2, \dots, \mathbf{z}^L\}$ given the current values of the error neurons. These two steps are then repeated for several iterations, specifically over a stimulus window of T steps, to arrive at a set of internal representations that accurately represent the input. This means that each layer/region ℓ of a neural coding model tries to satisfy two main objectives: 1) to uncover better latent representations in order to predict a nearby neural region/layer (a bottom-up adjustment), and 2) to be closer to what the layer above (\mathbf{z}^{l+1}) predicted its state should be (a top-down expectation). By performing several iterations of top-down prediction followed by state correction, the model not only minimizes layer-specific predictions but also optimizes its global (system) representation for the current dataset. Implementation details of the above processes, specifically generalized to the case of feature maps and (de)convolution, are provided in next in Section 3.

3 Neural Coding Training and Inference

In this section, we provide concrete implementation details of the neural coding process described earlier, depicting how layer-wise state prediction, state-correction, and synaptic parameter updating occur specifically in the context of visual object reconstruction. The first two steps iteratively predict and correct the representations of the Conv-NGC model for observed input values (natural images) of the current dataset. After T iterations, the final step entails adjusting model synaptic efficacies using simple Hebbian-like updates. In this section, we provide details of the three above steps and then describe the objective function that our model dynamically optimizes.

3.1 Inference: Predicting and Correcting Neural States

The full algorithm for both the prediction and correction steps of Conv-NGC is presented in Algorithm 1 and an example 3-layer Conv-NGC model is visually depicted in Figure 2. For each layer of a Conv-NGC system, note that the full state of any given layer ℓ is represented by a set of C_ℓ feature state maps, i.e., $\{\mathbf{z}_1^\ell, \mathbf{z}_2^\ell, \dots, \mathbf{z}_{C_\ell}^\ell\}$ where

¹Note that these predictions and error neuron calculations, even though presented in this work as occurring sequentially, can naturally be made in parallel given that they only depend on values immediately available to the relevant neurons.

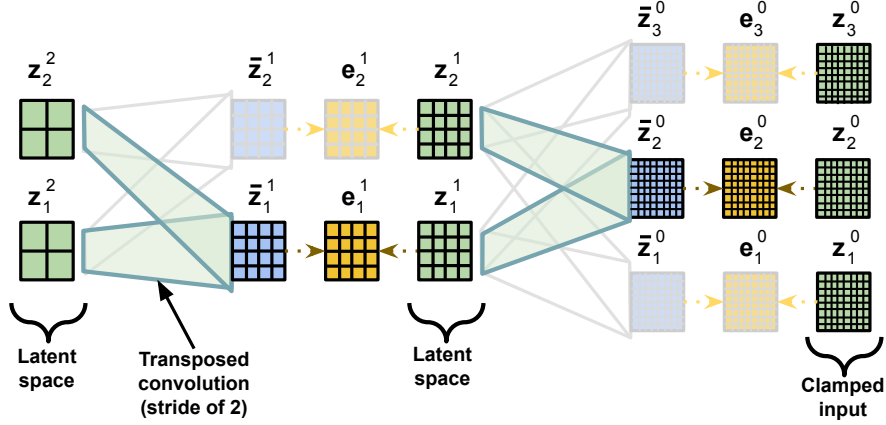


Figure 2: Depicted is a 3-layer convolutional neural generative coding network (Conv-NGC). Each latent state map \mathbf{z}_i^ℓ generates a prediction of each latent map $\mathbf{z}_j^{\ell-1}$ in the layer below via deconvolution (transposed convolution). In non-transparent colors, one possible prediction pathway in the Conv-NGC circuit is depicted (transparent colors indicate no involvement in this computational pathway), i.e., state maps \mathbf{z}_1^2 and \mathbf{z}_2^2 each contribute to the prediction $\bar{\mathbf{z}}_1^1$ of map \mathbf{z}_1^1 while state maps \mathbf{z}_1^1 and \mathbf{z}_2^1 each contribute to the prediction $\bar{\mathbf{z}}_2^0$ of map \mathbf{z}_2^0 (for example, since it is the bottom input layer, the \mathbf{z}_2^0 map could represent the red color channel of an input image space). Note that error unit map \mathbf{e}_1^1 encodes the mismatch between prediction $\bar{\mathbf{z}}_1^1$ and the actual value of latent map \mathbf{z}_1^1 while error unit map \mathbf{e}_2^0 computes the mismatch between prediction map $\bar{\mathbf{z}}_2^0$ and the value of latent map \mathbf{z}_2^0 . Green squares depict latent unit maps, blue squares depict prediction output maps, and orange/yellow squares depict error unit maps.

each state map \mathbf{z}_i^ℓ is essentially a block/cluster of neurons (that aim to encode a partial distributed representation of the detected input below), meaning that any layer consists of C_ℓ channels. To initialize each state map, instead of setting each to be grid of zero values (similar to how neural state vectors are initialized in fully-connected predictive coding models [37]), we initialize the states with a top-down ancestral projection pass by first sampling a random noise value for the top-most set of latent state maps, i.e., $\mathbf{z}_c^L \sim \mathcal{N}(\mu_z, \sigma_z)$, $c = 1, \dots, C_L$ (we set $\mu_z = 5$ and $\sigma_z = 0.05$ in this work), and then project the sampled state down along the Conv-NGC network to obtain the initial values of the other layers (see the start of Algorithm 1 for the specific details of this ancestral pass).

Layer-wise State Map Prediction: At each layer, the i th feature map state $\mathbf{z}_i^{\ell+1}$ is used to (partially) predict the j th feature map state of the layer below it, producing the prediction vector $\bar{\mathbf{z}}_j^{\ell+1}$. These local layer-wise predictors perform their computation independently (in parallel) and are coordinated through error units at each layer ℓ for each feature map. Specifically, the error neurons $\mathbf{e}_j^{\ell+1}$ at the layer $\ell + 1$ (for the j th channel) compute the difference between the prediction $\bar{\mathbf{z}}_j^{\ell+1}$ (from the layer ℓ above) and the target map activity $\mathbf{z}_j^{\ell+1}$. This error message/signal, in turn, is used to (partially) adjust the state representation \mathbf{z}^ℓ at layer ℓ (see Section Figure 2). Formally, the predictor and error neurons (in a convolutional/deconvolutional layer) are computed on a per-feature map basis as follows:

$$\bar{\mathbf{z}}_j^{\ell+1} = g^\ell \left(\left(\sum_i^{C_\ell} \mathbf{W}_{ij}^\ell \odot_s \phi^\ell(\mathbf{z}_i^\ell) \right) + \mathbf{b}_j \right), \quad \mathbf{e}_j^{\ell+1} = (\mathbf{z}_j^{\ell+1} - \bar{\mathbf{z}}_j^{\ell+1}), \quad (1)$$

where $\phi^\ell()$ is the nonlinear activation/transfer activation applied to the state activity map \mathbf{z}_i^ℓ , \mathbf{W}_{ij}^ℓ is the j th learnable kernel for the i th input state map, and \mathbf{b}_j is the j th bias map applied to the prediction/output map $\bar{\mathbf{z}}_j^\ell$. $g^\ell()$ is the predictive output nonlinearity applied to the result $\bar{\mathbf{z}}_j^\ell$ (typically chosen according to the distribution that is chosen to model the state of $\ell - 1$, e.g., the identity for a multivariate Gaussian model). Note that in the above equation, in a (de)convolutional layer, a final complete prediction of the j th output channel involves the summation/aggregation of multiple filters applied to each (input) state feature map of layer ℓ (up to C_ℓ input channels). Extending the prediction operation of Equation 1 to make use of stacks of operations, such as those that compose a residual block, is detailed in the Appendix (where we present a simple biologically-plausible scheme for handling credit assignment within a block of operations).

State Map Correction: During this step, the (i -th) state feature map \mathbf{z}_i^ℓ is refined using the values of the error neurons of the current and previous layers, i.e., ℓ and $\ell - 1$. For the top-most layer, the error \mathbf{e}_i^ℓ of any feature

²If a vector representation of the complete state is desired, then the concatenation of all C (flattened) feature map states/channels would make up the whole state, i.e., $\mathbf{z}^\ell = [\mathbf{z}_1^\ell, \mathbf{z}_2^\ell, \dots, \mathbf{z}_C^\ell]$.

Algorithm 1 Conv-NGC state prediction and correction.

```

1: Input: Data sample  $(\mathbf{x}, \mathbf{y})$ ; model parameters  $\Theta$ ; constants  $\beta, \gamma$ , and  $T$ 
2: Output: Corrected states/maps  $\{\mathbf{z}^0, \mathbf{z}^1, \mathbf{z}^2, \dots, \mathbf{z}^L\}$ ; error units/groups  $\{\mathbf{e}^0, \mathbf{e}^1, \dots, \mathbf{e}^L\}$ 
3: // Initialize system with an ancestral (top-down) projection pass
4:  $\mathbf{z}_c^L \sim \mathcal{N}(\mu_z, \sigma_z)$ ,  $c = 1, \dots, C_L$  and  $\mathbf{e}_c^L = \mathbf{0}$ ,  $c = 1, \dots, C_L$ 
5: for layer  $\ell = L - 1$  to  $0$  do
6:   for filter  $c = 1$  to  $C_\ell$  do ▷ For each output filter in layer  $\ell$ 
7:      $\mathbf{z}_c^\ell = \mathbf{0}$ 
8:     for filter  $i = 1$  to  $C_{\ell+1}$  do ▷ For each input filter in layer  $\ell + 1$ 
9:        $\bar{\mathbf{z}}_c^\ell \leftarrow \bar{\mathbf{z}}_c^\ell + \left( \mathbf{W}_{ic}^{(\ell+1)} \odot_s \phi^{\ell+1}(\mathbf{z}_i^{(\ell+1)}) \right)$  ▷ Partially compose state map of layer below
10:     $\mathbf{z}_c^\ell = \bar{\mathbf{z}}_c^\ell = g^{\ell+1}(\bar{\mathbf{z}}_c^\ell + \mathbf{b}_c^{\ell+1})$ 
11: // Simulate iterative processing over stimulus window of length  $T$ 
12:  $\mathbf{z}^0 = \mathbf{x}$  ▷ Clamp bottom-layer to image (set each channel of  $\mathbf{z}^0$  equal to each channel of  $\mathbf{x}$ )
13: for  $t = 1$  to  $T$  do
14:   for layer  $\ell = L - 1$  to  $0$  do
15:     // Run layer-wise predictors (per state feature map)
16:      $\bar{\mathbf{z}}_c^\ell = \mathbf{0}$ ,  $c = 1, \dots, C_\ell$ 
17:     for filter  $c = 1$  to  $C_\ell$  do ▷ For each filter in layer  $\ell$ 
18:       for channel  $i = 1$  to  $C_{\ell+1}$  do ▷ For each input channel in layer  $\ell$ 
19:          $\bar{\mathbf{z}}_c^\ell \leftarrow \bar{\mathbf{z}}_c^\ell + \left( \mathbf{W}_{ic}^{(\ell+1)} \odot_s \phi^{\ell+1}(\mathbf{z}_i^{(\ell+1)}) \right)$  ▷ Update output channel/prediction  $c$  of layer  $\ell$ 
20:        $\bar{\mathbf{z}}_c^\ell = g^{\ell+1}(\bar{\mathbf{z}}_c^\ell + \mathbf{b}_c^{\ell+1})$ ,  $\mathbf{e}_c^\ell = (\mathbf{z}_c^\ell - \bar{\mathbf{z}}_c^\ell)$  ▷ Calculate layer-wise error units (per feature map)
21:     // Correct internal states (per state feature map)
22:      $\mathbf{d}_c^{\ell+1} = \mathbf{0}$ ,  $c = 1, \dots, C_{\ell+1}$ 
23:     for channel  $i = 1$  to  $C_{\ell+1}$  do ▷ For each input channel in  $\ell + 1$ , compute (total) perturbation
24:       for channel  $c = 1$  to  $C_\ell$  do ▷ For each output (error) channel in layer  $\ell$ 
25:          $\mathbf{d}_i^{\ell+1} \leftarrow \mathbf{d}_i^{\ell+1} + (\mathbf{E}_{ci}^{\ell+1} *_s \mathbf{e}_c^\ell)$ 
26:          $\mathbf{d}_i^{\ell+1} = \mathbf{d}_i^{\ell+1} - \mathbf{e}_i^{\ell+1}$  and  $\mathbf{z}_i^{\ell+1} \leftarrow (\mathbf{z}_i^{\ell+1} + \beta \mathbf{d}_i^{\ell+1} - \gamma \mathbf{z}_i^{\ell+1})$ 
27: Return:  $\{\mathbf{z}^0, \mathbf{z}^1, \mathbf{z}^2, \dots, \mathbf{z}^L\}$ ,  $\{\mathbf{e}^0, \mathbf{e}^1, \dots, \mathbf{e}^{L-1}\}$  ▷ Output system statistics

```

map i does not exist so it is not computationally modeled/simulated. Formally, the ℓ -th predictor (or rather, its i th map \mathbf{z}_i^ℓ) corrects its state values using both the bottom-up and top-down error messages/signals according to the following (Euler) integration scheme below:

$$\mathbf{z}_i^\ell \leftarrow (\mathbf{z}_i^\ell + \beta \mathbf{d}_i^\ell - \gamma \mathbf{z}_i^\ell), \text{ where } \mathbf{d}_i^\ell = -\mathbf{e}_i^\ell + \sum_j^{C_{\ell-1}} \mathbf{E}_{ji}^\ell *_s \mathbf{e}_j^{\ell-1}, \quad (2)$$

where \leftarrow denotes a variable override and the modulation/adjustment factor β is a constant value, which controls the state correction rate, and $-\gamma \mathbf{z}_i^\ell$ is the leak variable, controlled by the strength factor γ (set to a small value such as 0.001, also serving as a form of light regularization applied to the latent state map neurons). The (4D) error kernel tensor \mathbf{E}^ℓ models a learnable feedback pathway that is responsible for transmitting the error from the layer $\ell - 1$ to the layer ℓ . This means that the bottom-up error message/perturbation is produced by aggregating across the $C_{\ell-1}$ output channels/state maps that make up layer $\ell - 1$, i.e., a convolution must be applied to each output channel j as follows: $\mathbf{E}_{ji}^\ell *_s \mathbf{e}_j^{\ell-1}$, meaning that the prediction of each lower-level state map that was (partially) made by the state map/predictor \mathbf{z}_i^ℓ contributes equally to its final, resulting in a state map correction (which is further modulated by the top-down pressure \mathbf{e}_i^ℓ , exerted by the layer above $\mathbf{z}^{\ell+1}$). Although having separate error kernels for transmitting error message signals resolves the weight transport problem that characterizes backprop-based learning (and is thus more biologically plausible), this comes at an increased memory cost/footprint and additional computation that is needed for updating the error filters themselves. Thus, we set the error filters, in this work, to be $\mathbf{E}_{ji}^\ell = (\mathbf{W}_{ij}^\ell)^T$, to speed up simulation (not observing any noticeable change in performance).

Note that, at test time, for inference, we use Algorithm 1 without adjusting synaptic efficacies, either clamping or initializing the bottom state $\mathbf{z}^0 = \mathbf{x}$. To obtain a prediction, the neural system will iterate through T steps of state prediction and correction, eventually outputting $\bar{\mathbf{z}}^0$.

Algorithm 2 Conv-NGC synaptic adjustment (given statistics from Algorithm 1).

```

1: Input: State maps  $\{\mathbf{z}^0, \mathbf{z}^1, \mathbf{z}^2, \dots, \mathbf{z}^L\}$ ; error maps  $\{\mathbf{e}^1, \mathbf{e}^2, \dots, \mathbf{e}^L\}$ ; model parameters  $\Theta$ ;
2:   Constants  $\lambda, \alpha, \gamma, \epsilon$ 
3: Output: Updated  $\Theta$ 
4: for layer  $\ell = 1$  to  $L$  do
5:   // Calculate synaptic adjustments/displacements
6:   for layer  $c = 1$  to  $C_\ell$  do ▷ For each filter in layer  $\ell$ 
7:      $\Delta \mathbf{W}_{ic}^\ell = \mathbf{0}, \Delta \mathbf{E}_{ci}^\ell = \mathbf{0}$ 
8:     for layer  $i = 1$  to  $C_{\ell-1}$  do ▷ For each input (error) channel of layer  $\ell - 1$ 
9:        $\Delta \mathbf{W}_{ic}^\ell \leftarrow \Delta \mathbf{W}_{ic}^\ell + \mathbf{e}_c^{\ell-1} *_1 \text{Dilate}\left((\phi^\ell(\mathbf{z}_i^\ell))^T, s\right)$ 
10:       $\Delta \mathbf{E}_{ci}^\ell \leftarrow \Delta \mathbf{E}_{ci}^\ell + \lambda \left( \text{Dilate}\left((\phi^\ell(\mathbf{z}_i^\ell))^T, s\right) *_1 \mathbf{e}_c^{\ell-1} \right)$ 
11:     // Update current filter synapses – could alternatively use Adam [25] or RMSprop [59]
12:      $\mathbf{W}_{ic}^\ell \leftarrow \mathbf{W}_{ic}^\ell - \alpha (\Delta \mathbf{W}_{ic}^\ell / (\|\Delta \mathbf{W}_{ic}^\ell\|_2 + \epsilon))$  and  $\mathbf{E}_{ci}^\ell \leftarrow \mathbf{E}_{ci}^\ell - \gamma (\Delta \mathbf{E}_{ci}^\ell / (\|\Delta \mathbf{E}_{ci}^\ell\|_2 + \epsilon))$ 
13: Return:  $\Theta = \{ \{ \{ \mathbf{W}_{ic}^\ell, \mathbf{E}_{ci}^\ell \}_{i=1}^{C_\ell} \}_{c=1}^{C_{\ell-1}} \}_{\ell=1}^L$  ▷ Output newly adjusted synaptic efficacies

```

3.2 Training: Updating Model Parameters

After T iterations of state prediction and correction (or application of Algorithm 1), a Conv-NGC model then updates its synaptic weights. The full process underlying this phase is described in Algorithm 2.

Neural Coding Synaptic Update. The updates to each state prediction filter \mathbf{W}_{ij}^ℓ and error filter \mathbf{E}_{ji}^ℓ are computed according to a Hebbian-like update (based on the principle of local representation alignment (LRÄ) [42]):

$$\Delta \mathbf{W}_{ij}^\ell = \mathbf{e}_j^{\ell-1} *_1 \text{Dilate}\left((\phi^\ell(\mathbf{z}_i^\ell))^T, s\right), \quad \Delta \mathbf{E}_{ji}^\ell = \lambda \left(\text{Dilate}\left((\phi^\ell(\mathbf{z}_i^\ell))^T, s\right) *_1 \mathbf{e}_j^{\ell-1} \right)$$

where λ is modulation factor meant to control the time scale of the evolution of the error filters (and generally set to be less than one, e.g., 0.9) - note that this update rule is discarded if $\mathbf{E}_{ji}^\ell = (\mathbf{W}_{ij}^\ell)^T$ as we do in this work. Note that the above local update rule is a generalization of the rule proposed in [39, 37] to the case of a (de)convolutional filter. After the update for any particular filter has been calculated and it has been used to adjust the current physical state of the kernel synapses, we further normalize/constrain each kernel such that its Euclidean norm does not exceed one (see Algorithm 2 for the specific re-projection step). This constraint ensures that Conv-NGC avoids the degenerate/trivial solution of simply increasing its synaptic kernel values while obtaining only small/near-zero latent activity values, much as is done in convolutional sparse coding [19] (this also means that one could alternatively view Conv-NGC as a sort of “deep” convolutional sparse coding).

3.3 Objective Function

During training, a Conv-NGC model refines its internal states such that the output of the local predictions move as close as possible to the actual values of the state maps, further meaning that the bottom-most layer stays as close as possible to the input image pattern \mathbf{x}_j . In order to do this, Conv-NGC attempts to optimize the *total discrepancy optimization* (ToD) function [41, 42, 37] via the prediction, state correction, and synaptic adjustment steps presented in the earlier sub-sections. The simplest version of this optimization function is defined as the sum of mismatches between the predictions and actual states at each level of the model:

$$\mathcal{L}_{ToD} = \sum_{\ell} \left(-\frac{1}{2} \|\mathbf{z}^\ell - \bar{\mathbf{z}}^\ell\|_q^p \right), \text{ where, } p = q = 2. \quad (3)$$

The online minimization of the discrepancy among states as depicted in Equation 3 progressively refines the representation of all layers in our model. Notably, the total discrepancy objective can also be viewed as approximately minimizing a form of (variational) free energy [13], representing a concrete statistical learning connection to and implementation of a prominent neuro-mechanistic Bayesian brain theory.

4 Experiments

Given our specification of the Conv-NGC model’s inference and learning processes, we next describe our experimental setup, including descriptions of the baseline models we compare against, the natural image datasets and evaluation metrics utilized, and the tasks simulated.

4.1 Baseline Models

Convolutional Autoencoder: As our first baseline, we designed a convolution auto-encoder (Conv-AE) to compare against our Conv-NGC decoder-only model. The Conv-AE consists of five blocks in encoder, where one block is comprised of a convolution layer (with 32 output feature maps, 3×3 kernel, “SAME” padding, and a stride of 2) followed by a relu activation, batch normalization and finally a max-pooling layer (also with a stride of 2). The latent space/bottleneck layer is then passed through multiple layers of deconvolution in order to reconstruct the input. The AE models were trained using Adam with a step size of $2e - 5$ (mini-batches used to estimate gradients were of size 128) with weights initialized using glorot initialization. The output layer of the decoder made use of a logistic sigmoid activation. Conv-AEs have total of 48,393 trainable parameters in order to learn the distribution of each benchmark.

Convolutional Denoising Autoencoder: Beyond the Conv-AE, we designed a convolutional denoising autoencoder (Conv-DAE), which follows the same design principle as the Conv-AE, with the key difference that we inject noise into the input data (in order to make model robust against noise). This noise injection process also helps the DAE to better reconstruct inputs by averaging over pixels to create a smoother output. Another notable alteration made to the Conv-DAE was that the selu activation function was used instead of the relu. Based on preliminary experimentation, we observed that replacing relu with selu resulted in overall better reconstruction for Conv-DAEs. Conv-DAEs have a total of 48,393 trainable parameters in order to learn the distribution of each benchmark.

Neural Generative Coding: We also experimented with the fully-connected form of neural generative coding (NGC), which, when the error feedback synaptic matrices are set to be equal to the transpose of the forward generative synaptic matrices and the derivative of the activation is used in the latent state update, we recover the unsupervised form of the model in [51] (also referred to as the hierarchical predictive coding network, or PCN). For all datasets studied, the NGC model we crafted contained five state layers (the bottom layer was sized to be the same shape as the input image) where each layer contained 200 neurons and employed a leaky rectifier activation for $\phi^\ell(\mathbf{v})$ with generative synapses initialized from a zero-mean Gaussian distribution and standard deviation of 0.1 (biases were initialized to zero vectors). The output prediction activation were set to be the identity, i.e., $g^\ell(\mathbf{v}) = \mathbf{v}$, except for the bottom layer ($g^0(\mathbf{v})$), which was set to be the logistic sigmoid. The NGC model’s stimulus window was set to be of length $T = 60$ and a state update rate of $\beta = 0.1$ was used. Latent state vector values were sampled from a Gaussian distribution $\mathcal{N}(0.5, 0.05)$ (meaning at the first step of the stimulus window, they were non-zero). Synaptic parameters were adjusted using the Adam adaptive learning rate with step size 0.001 with mini-batches of size 500. In accordance with [37] and with proper sparse coding practice, we constrained the L2 norms of the columns of the synaptic matrices to have values no greater than one. Note that, for predicting $32 \times 32 \times 3$ color images, our NGC models utilized 738,072 total free parameters to learn the distribution of each benchmark (considerably more synaptic parameters than the convolutional autoencoder models).

Convolutional Neural Generative Coding: For convolutional neural generative coding (Conv-NGC), for all datasets, we designed all models to contain five layers of state maps, where each layer/block leveraged deconvolution with a stride set to $s = 2$ (kernel size was 3×3 using “SAME” padding), meaning that each map in the top-most latent state layer was of size 2×2 neurons and increased in size until reaching a size of 32×32 at the bottom layer (where each map in the bottom-most layer, which is normally be clamped to an input image color channel, would also be of size 32×32). The channel configuration of our Conv-NGC decoder-only model is $\{10, 15, 20, 25, 3\}$ (going from left to right gives the number of channels starting from the top-most latent state layer, where the rightmost value should be equal to the number of color channels that define a natural image). The state activation function $\phi^\ell()$ was set to be the leaky rectifier while the local prediction activation $g^\ell()$ was set to be the identity (for all layers including the bottom-most layer). Synapses were initialized from a zero-mean Gaussian distribution with a standard deviation of 0.1 (bias maps were initialized to zero values). The Conv-NGC model’s stimulus window was set to a length of $T = 60$ and a state map update rate of $\beta = 0.1$ was used. The top-most latent state maps were sampled from a Gaussian distribution $\mathcal{N}(0.5, 0.05)$ while the rest were initialized from the top-down ancestral sampling pass (shown in the first part of Algorithm 1). Synaptic matrices were adjusted using Adam with a step size of 0.001 using mini-batches of size 500. In contrast to the NGC models, Conv-NGC utilized a total of 9,225 free parameters in order to learn the distribution of each benchmark (note that if separate error filters were used, this would only double the parameter count to a mere 18,450 synapses), considerably fewer parameters than the NGC and autoencoder models. Finally, note that in the case of denoising, the bottom-most units/state maps of both NGC and Conv-NGC were only clamped to the input image(s) at the first time step $t = 1$ of the stimulus and allowed to evolve according to the dynamics of Equation 2.

4.2 Datasets

We next describe the data benchmarks that were used to evaluate Conv-NGC and the relevant baseline systems. The first three, Color MNIST, CIFAR-10, and SVHN, were utilized in both training and testing/evaluation contexts while the fourth one, CINIC-10, was only used (as a test set) for the out-of-distribution reconstruction experiments.

Color-MNIST: Color-MNIST is the colored version of the MNIST dataset with 60,000 training and 10,000 test samples. We resize Color-MNIST images to 32×32 using linear interpolation. In the original MNIST, the images are grayscale; in the colored form of MNIST, each image is either red or green. This database is designed to correlate strongly (though spuriously) with the class label. Thus, by construction, the label is more strongly correlated with the color than with the digit, so any algorithm purely minimizing training error will likely exploit the color. Such approaches will fail at test time because the direction of the correlation is reversed in the test environment, which makes this dataset a challenging benchmark.

The CIFAR-10 Dataset: The CIFAR-10 dataset has 50,000 training and 10,000 test images, across 10 categories including those depicting animals and vehicles. Images are of size 32×32 pixels. 5,000 training samples were set aside to measure validation metrics and tune hyper-parameters.

The Street View House Numbers (SVHN) Dataset: The SVHN dataset has approximately 75,000 training and 23,000 test images. All images are of size $32 \times 32 \times 3$ pixels. We randomly select 5,000 from all 10 classes to create validation set to perform hyper-parameter optimization.

The CINIC-10 Dataset: The CINIC-10 dataset is a more challenging alternative to CIFAR-10 and contains a total of 270,000 natural color images, nearly 4.5 times that of the size of CIFAR-10. The CINIC database is ultimately built from two data sources, i.e., ImageNet and CIFAR-10. The data is further split into three equal subsets, i.e., a training, validation, and testing partition, where each contains 90,000 images. (As noted earlier, we only use its test-set for the out-of-distribution prediction experiments later.)

4.3 Reconstruction and Denoising

In this set of tasks, we investigate each model’s ability to reconstruct the given input image patterns from each dataset as well as to recover the original input image values under corruption noise. For the task of reconstruction, we measure the mean squared error (MSE) for each input between the model’s predicted/output values $\hat{\mathbf{x}}_i$ and the original image \mathbf{x}_i as follows:

$$\text{MSE}(\mathbf{x}_i, \hat{\mathbf{x}}_i) = \frac{1}{I} \sum_{i=1}^I \left(\frac{1}{C} \sum_{c=1}^C \left(\frac{1}{N * M} \sum_{n=1}^N \sum_{m=1}^M (\hat{\mathbf{x}}_{nmci} - \mathbf{x}_{nmci})^2 \right) \right) \quad (4)$$

which is calculated per channel $c \in C$ and then averaged over all channels and images in the test set. To better probe the image quality of the reconstructed outputs, we evaluate the structural similarity index measure (SSIM):

$$\text{SSIM}(\mathbf{x}_i, \hat{\mathbf{x}}_i) = \frac{(2\mu_{x_i}\mu_{\hat{x}_i} + (0.01Q)^2)(2\sigma_{x_i\hat{x}_i} + (0.03Q)^2)}{(\mu_{x_i}^2 + m\mu_{\hat{x}_i}^2 + (0.01Q)^2)(\sigma_{x_i}^2 + \sigma_{\hat{x}_i}^2 + (0.03Q)^2)} \quad (5)$$

where μ_{x_i} and $\mu_{\hat{x}_i}$ are the pixel sample means for the original image \mathbf{x}_i and reconstruction $\hat{\mathbf{x}}_i$, respectively, and σ_{x_i} and $\sigma_{\hat{x}_i}$ are the pixel standard deviations ($\sigma_{x_i\hat{x}_i}^2$ is the covariance between \mathbf{x}_i and $\hat{\mathbf{x}}_i$). Q is the dynamic range of the pixels, i.e., $Q = 2^{\text{bpc}} - 1$ (where bpc is bits-per-pixel).

Finally, for the more complex natural images in SVHN and CIFAR-10, we further measure peak signal-to-noise ratio (PSNR) formally defined as follows:

$$\text{PSNR}(\mathbf{x}_i, \hat{\mathbf{x}}_i) = \frac{1}{I} \sum_{i=1}^I \left(\frac{1}{C} \sum_{c=1}^C (20 \times \log_{10} (255.0 / (\sqrt{\frac{1}{N * M} \sum_{n=1}^N \sum_{m=1}^M (\hat{\mathbf{x}}_{nmci} - \mathbf{x}_{nmci})^2})) \right) \quad (6)$$

Out-of-Distribution Reconstruction: One interesting property of auto-encoding systems that we are interested in examining is their ability to reconstruct image pattern samples not seen in the original data distribution, particularly samples that come from a much different distribution (violating the i.i.d. assumption typical to fundamental statistical learning). To evaluate the out-of-distribution (OOD) reconstruction ability of our models, we take the trained models on the SVHN dataset (the source dataset) and evaluate their ability to reconstruct samples from the distinct CIFAR-10 dataset as well as the larger, more difficult CINIC-10 database (specifically evaluating predictive ability on their test sets). For the results of this OOD task, see Table 3.

Color-MNIST				
Model	Reconstruction		Denoising ($\sim \mathcal{N}(0, 0.1)$)	
	MSE	SSIM	MSE	SSIM
Conv-AE	32.99 ± 1.0680	0.9021 ± 0.0100	176.9321 ± 2.0923	0.6912 ± 0.007
Conv-DAE	23.09 ± 0.4722	0.9324 ± 0.0060	76.8610 ± 0.8511	0.8424 ± 0.003
NGC	328.5659 ± 3.5000	0.7652 ± 0.0032	887.205 ± 18.2500	0.5476 ± 0.0075
Conv-NGC	11.2802 ± 0.5008	0.9838 ± 0.0005	202.2222 ± 1.0511	0.6732 ± 0.0006
CIFAR-10				
Model	Reconstruction		Denoising ($\sim \mathcal{N}(0, 0.1)$)	
	MSE	SSIM	MSE	SSIM
Conv-AE	13.6890 ± 1.6320	0.9310 ± 0.0030	208.4608 ± 9.3928	0.7628 ± 0.0003
Conv-DAE	8.8810 ± 1.5311	0.9720 ± 0.0010	16.7781 ± 5.1037	0.9110 ± 0.0020
NGC	413.5140 ± 7.1000	0.7230 ± 0.0003	913.2587 ± 21.2000	0.5308 ± 0.0025
Conv-NGC	6.3668 ± 1.2522	0.9955 ± 0.0009	183.8624 ± 9.4002	0.8603 ± 0.0007
SVHN				
Model	Reconstruction		Denoising ($\sim \mathcal{N}(0, 0.1)$)	
	MSE	SSIM	MSE	SSIM
Conv-AE	7.5043 ± 2.9351	0.8934 ± 0.0002	154.6783 ± 25.7555	0.7490 ± 0.0030
Conv-DAE	2.7263 ± 1.9286	0.9510 ± 0.0002	87.9926 ± 7.2091	0.9002 ± 0.0030
NGC	67.393 ± 9.02	0.9436 ± 0.0028	1116.764 ± 283.55	0.6704 ± 0.0904
Conv-NGC	1.9500 ± 0.5609	0.9976 ± 0.0002	97.2695 ± 3.5245	0.8650 ± 0.0007

Table 1: Model reconstruction and denoising performance on the test samples of Color-MNIST (top), CIFAR-10 (middle), and SVHN (bottom). Reported measurements are mean and standard deviation across five trials. (Note: model output values are re-scaled between 0-255 when calculating metrics.) In terms of performance, a lower MSE and higher SSIM are better.

CIFAR-10		
Model	Reconstruction	Denoising ($\sim \mathcal{N}(0, 0.1)$)
	PSNR	PSNR
Conv-AE	36.7872 ± 1.0056	24.6527 ± 0.2001
Conv-DAE	38.6462 ± 1.2033	36.4346 ± 0.2021
NGC	22.8462 ± 0.0400	19.0410 ± 0.1203
Conv-NGC	41.0912 ± 0.0234	25.9004 ± 0.2004
SVHN		
Model	Reconstruction	Denoising ($\sim \mathcal{N}(0, 0.1)$)
	PSNR	PSNR
Conv-AE	39.3777 ± 0.2000	26.2369 ± 0.3000
Conv-DAE	43.7750 ± 0.3000	28.6864 ± 0.2000
NGC	33.2763 ± 1.0800	19.8709 ± 2.0800
Conv-NGC	45.2305 ± 0.0800	28.2513 ± 0.1600

Table 2: Peak signal-to-noise ratio (PSNR; a higher value is better) analysis of model reconstruction and denoising ability (mean and standard deviation are calculated over five trials) on the test set image samples of the CIFAR-10 database (top) and the SVHN database (bottom).

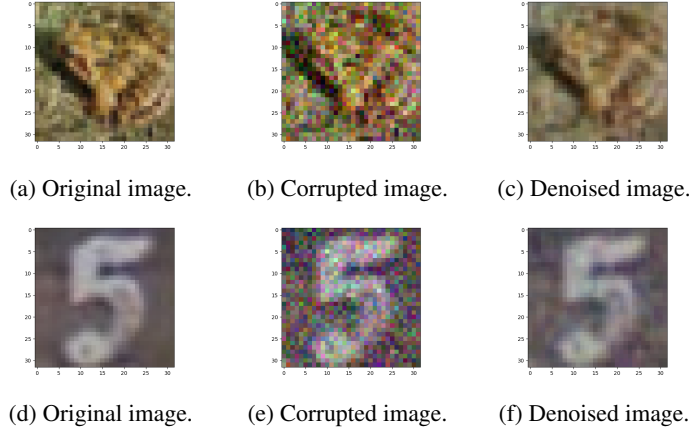


Figure 3: Example image randomly sampled from the dataset test set (Left), the same image corrupted with noise $\sim \mathcal{N}(0, 0.1)$ (Middle), and the Conv-NGC denoised image given the corrupted pattern (Right). Top row shows a sample taken from CIFAR-10 dataset while the bottom row shows a sample taken from the SVHN database.

Model	SSIM	SVHN to CIFAR-10	
		PSNR	MSE
Conv-AE	0.6892 ± 0.0010	24.0331 ± 0.2577	387.02 ± 7.8230
Conv-DAE	0.7712 ± 0.0002	29.4589 ± 0.3666	175.999 ± 5.0871
Conv-NGC	0.9804 ± 0.0006	35.0341 ± 0.3031	26.7894 ± 2.0045
Model	SSIM	SVHN to CINIC-10	
		PSNR	MSE
Conv-AE	0.7002 ± 0.0050	23.7361 ± 0.3090	275.0870 ± 8.0200
Conv-DAE	0.7380 ± 0.0020	27.0961 ± 0.5020	127.8900 ± 4.5500
Conv-NGC	0.9674 ± 0.0013	32.5431 ± 0.2001	47.8363 ± 2.5000

Table 3: Out-of-distribution reconstruction performance results. Measurements (mean and standard deviation) of SSIM, PSNR, and MSE are over five experimental trials. Lower MSE and higher SSIM and PSNR are better.

4.4 Discussion

As seen in our results, Conv-NGC outperforms NGC (or the PCN, as expected) and exhibits competitive behavior with the backprop-based autoencoder models. Notably, in terms of reconstruction, Conv-NGC even offers improved SSIM and PSNR, which is likely the result of its ability to learn a reconstruction process (over a T -length window of time). With respect to image denoising, we observe that the Conv-NGC models works well, outperforming both the AE and NGC models specifically on the harder natural image datasets (CIFAR-10 and SVHN), but under-performs the DAE. The DAE, however, was trained directly for the task of denoising (with noise injected to its input nodes), so it makes sense that it would outperform models that were not tuned to the task (and thus serves well as a soft upper bound on performance). See Figure 3 for visual examples of image samples that the Conv-NGC model denoised (for CIFAR-10 and SVHN).

Note that, for the table metrics reported, pixel reconstruction/model output values were re-scaled between 0 – 255, which highlighted a broader gap between results obtained for Conv-NGC and other baseline models. More importantly, Conv-NGC exhibits a low variance and better visual reconstruction/modeling comparatively as indicated by SSIM, which is a metric that more closely relates to / correlates with human perception. To probe the knowledge acquired in the Conv-NGC’s distributed representations, we also examined the learned latent state feature maps of the trained Conv-NGC on sampled test images samples taken from each of the data benchmarks. Qualitatively, we observe that Conv-NGC appears to implicitly learns a (noisy) form of the image pyramid [1] within its latent activities. See Figure 4 for visual samples of the feature maps for the bottom three latent states, including the bottom layer which was clamped to a natural image input (we present the first eight maps of each layer and all three channels of the input state layer). In each triplet of rows in Figure 4, we see that, going from bottom row to top row, the sensory image appears in some of the feature state maps, but is a down-sampled, decreased resolution form of itself (much akin to the repeated process of smoothing and sub-sampling that results in lower

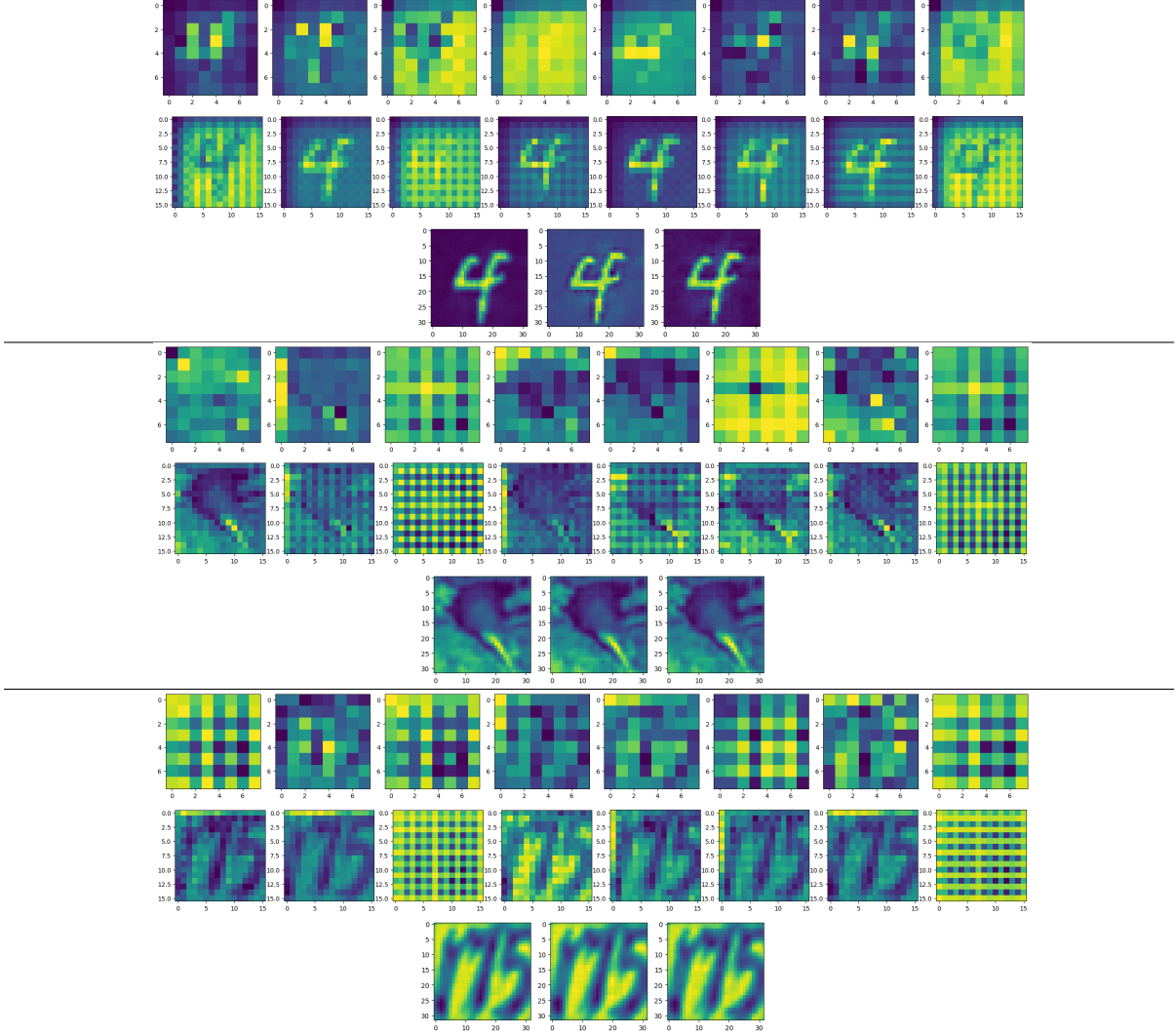


Figure 4: Features maps extracts from bottom three layers/levels of a trained Conv-NGC model. (Top 3) Color MNIST feature state maps, (Middle 3) Cifar feature state maps, and (Bottom 3) SVHN feature state maps. For each group of three rows, the bottom row shows the clamped input, the middle shows the first latent state map layer, and the top shows the second highest latent state map layer.

spatial density images the higher up one goes within the image pyramid). This result complements early work that highlighted the notion that the brain processes visual information at different resolutions [6]. This biological multi-resolution analysis of the world allows the brain to extract useful information from typically complex input patterns and it appears that Conv-NGC implicitly learns to conduct a similar type of analysis on the static natural images that it observes in the Color MNIST, CIFAR-10, and SVHN benchmarks.

Surprisingly, with respect to the OOD experiments, Conv-NGC outperforms all of the baselines (including the DAE), further corroborating the in-dataset reconstruction result(s) that Conv-NGC appears to (meta-)learn a type of reconstruction process that works well on unseen, out-of-distribution natural image patterns. This improvement is indicated by the higher trial-averaged (OOD) PSNR as well as the (OOD) SSIM score on both problem settings: 1) SVHN-to-CIFAR-10 reconstruction, and 2) SVHN-to-CINIC-10 reconstruction. What is impressive is that the Conv-NGC model was trained on natural images that did not contain any of the objects depicted in either CIFAR-10 and CINIC-10 and was still able to reconstruct with top performance. This result offers a promising future direction worth exploring for Conv-NGC/NGC predictive coding systems in general – their ability to generalize to unseen sample patterns that are more likely violate the assumption that they were generated by a distribution similar to that of the training data.

5 Related Work

Predictive Coding: The motivation behind our model’s design and learning procedure is grounded in predictive coding principles [45]. According to predictive coding theory [57, 4, 47, 13], at each level of a cognitive process, the brain continuously generates and updates beliefs about what information its internal model of the world should be receiving from the level above it. These beliefs get translated into predictions, which are the best possible explanations of what is perceived/observed, such that the system’s overall (sensory) experience makes sense [44]. Sparse predictive coding models [34, 47] embody the hypothesis that the brain is a type of directed generative model, combining top-down prediction and bottom-up signals/messages in order to facilitate dynamic adaptation to its environment [48]. This forms a type of iterative inference that progressively corrects latent distributed representations. Furthermore, when nesting the ideas of predictive coding within the Kalman Filter framework [46], one can create dynamic models that handle time-varying data. Many variations and implementations of predictive coding have been developed [7, 8, 28, 53, 22, 56, 39, 38, 52]. Some of the more recent ones merge it with back-propagation of errors as a subsequent fine-tuning step and speed up training [31, 35]. Nevertheless, most prior work on predictive coding networks (with notable exceptions such as [58]), in general, focuses on neural coding blocks implemented as fully connected layers [61, 51, 37, 15] while others that do utilize convolution adapt/modify backprop-based networks to utilize principles of predictive coding [28, 16, 60, 9]. In this work, we are the first to generalize predictive coding fully to the case of (de)convolution (and residual blocks as shown in the Appendix) for visual data processing, specifically facilitating the design of causal-like, decoder-only generative/reconstruction models of natural images.

Local Learning: One key concept behind predictive coding is that each neural architecture layer would need an error feedback mechanism to communicate its needs, i.e., activity mismatch signals transmitted to relevant nearby layers. Suppose the feedback signals come closer to the layers themselves. In this scenario, error connections can share information to the right units such that the discrepancy between learned representations and target representations is minimum. Such types of local updates are referred to as local learning approaches [42, 26, 33], which offer a potential replacement for back-propagation when training artificial neural networks. Empirically, updates from a more localized approach can lead to better generalization performance [26, 42]. Historically, there have been many efforts at crafting algorithms that learn locally, including those based on contrastive Hebbian learning [32], contrastive divergence for learning harmoniums [20], the wake-sleep algorithm for adapting Helmholtz machines [21], and, more recently, equilibrium propagation [54]. Other recent efforts, which more directly integrate local learning into the deep learning pipeline/modeling framework, include kickback [2] and decoupled neural interfaces [23].

6 Conclusion

In this work, we proposed convolutional neural generative coding (Conv-NGC), a generalization of a computational predictive coding framework to the case of natural images. Our experiments on three benchmark datasets, i.e., Color-MNIST, CIFAR-10, and SVHN, demonstrate that Conv-NGC is competitive with powerful backprop-based convolutional autoencoding models with respect to both pattern reconstruction and image denoising and outperforms all of them in the context of out-of-distribution reconstruction. Our results mark an important step towards crafting more robust, general brain-inspired neural architectures and learning processes capable of handling machine learning-scale tasks.

References

- [1] ADELSON, E. H., ANDERSON, C. H., BERGEN, J. R., BURT, P. J., AND OGDEN, J. M. Pyramid methods in image processing. *RCA engineer* 29, 6 (1984), 33–41.
- [2] BALDUZZI, D., VANCHINATHAN, H., AND BUHMANN, J. M. Kickback cuts backprop’s red-tape: Biologically plausible credit assignment in neural networks. In *AAAI* (2015), pp. 485–491.
- [3] BASTOS, A. M., USREY, W. M., ADAMS, R. A., MANGUN, G. R., FRIES, P., AND FRISTON, K. J. Canonical microcircuits for predictive coding. *Neuron* 76, 4 (2012), 695–711.
- [4] BRODSKI, A., PAASCH, G.-F., HELBLING, S., AND WIBRAL, M. The faces of predictive coding. *Journal of Neuroscience* 35, 24 (2015), 8997–9006.
- [5] BROWN, T., MANN, B., RYDER, N., SUBBIAH, M., KAPLAN, J. D., DHARIWAL, P., NEELAKANTAN, A., SHYAM, P., SASTRY, G., ASKELL, A., ET AL. Language models are few-shot learners. *Advances in neural information processing systems* 33 (2020), 1877–1901.

- [6] CAMPBELL, F. W., AND ROBSON, J. G. Application of fourier analysis to the visibility of gratings. *The Journal of physiology* 197, 3 (1968), 551.
- [7] CHALASANI, R., AND PRINCIPE, J. C. Deep predictive coding networks. *arXiv preprint arXiv:1301.3541* (2013).
- [8] CHALASANI, R., AND PRINCIPE, J. C. Context dependent encoding using convolutional dynamic networks. *IEEE Transactions on Neural Networks and Learning Systems* 26, 9 (Sep. 2015), 1992–2004.
- [9] CHOKSI, B., MOZAFARI, M., BIGGS O'MAY, C., ADOR, B., ALAMIA, A., AND VANRULLEN, R. Predify: Augmenting deep neural networks with brain-inspired predictive coding dynamics. *Advances in Neural Information Processing Systems* 34 (2021), 14069–14083.
- [10] CLARK, A. *Surfing uncertainty: Prediction, action, and the embodied mind*. Oxford University Press, 2015.
- [11] CRICK, F. The recent excitement about neural networks. *Nature* 337, 6203 (1989), 129–132.
- [12] FLORIDI, L., AND CHIRIATTI, M. Gpt-3: Its nature, scope, limits, and consequences. *Minds and Machines* 30, 4 (2020), 681–694.
- [13] FRISTON, K. The free-energy principle: a unified brain theory? *Nature reviews neuroscience* 11, 2 (2010), 127–138.
- [14] FURBER, S. Large-scale neuromorphic computing systems. *Journal of neural engineering* 13, 5 (2016), 051001.
- [15] GKLEZAKOS, D. C., AND RAO, R. P. Active predictive coding networks: A neural solution to the problem of learning reference frames and part-whole hierarchies. *arXiv preprint arXiv:2201.08813* (2022).
- [16] HAN, K., WEN, H., ZHANG, Y., FU, D., CULURCIELLO, E., AND LIU, Z. Deep predictive coding network with local recurrent processing for object recognition. *Advances in neural information processing systems* 31 (2018).
- [17] HE, K., ZHANG, X., REN, S., AND SUN, J. Delving deep into rectifiers: Surpassing human-level performance on imagenet classification. In *Proceedings of the IEEE international conference on computer vision* (2015), pp. 1026–1034.
- [18] HEBB, D. O., ET AL. The organization of behavior, 1949.
- [19] HEIDE, F., HEIDRICH, W., AND WETZSTEIN, G. Fast and flexible convolutional sparse coding. In *Proceedings of the IEEE Conference on Computer Vision and Pattern Recognition* (2015), pp. 5135–5143.
- [20] HINTON, G. E. Training products of experts by minimizing contrastive divergence. *Neural computation* 14, 8 (2002), 1771–1800.
- [21] HINTON, G. E., DAYAN, P., FREY, B. J., AND NEAL, R. M. The "wake-sleep" algorithm for unsupervised neural networks. *Science* 268, 5214 (1995), 1158–1161.
- [22] HWANG, J., KIM, J., AHMADI, A., CHOI, M., AND TANI, J. Dealing with large-scale spatio-temporal patterns in imitative interaction between a robot and a human by using the predictive coding framework. *IEEE Transactions on Systems, Man, and Cybernetics: Systems* (2018), 1–14.
- [23] JADERBERG, M., CZARNECKI, W. M., OSINDERO, S., VINYALS, O., GRAVES, A., AND KAVUKCUOGLU, K. Decoupled neural interfaces using synthetic gradients. *arXiv preprint arXiv:1608.05343* (2016).
- [24] KENDALL, J., PANTONE, R., MANICKAVASAGAM, K., BENGIO, Y., AND SCELLIER, B. Training end-to-end analog neural networks with equilibrium propagation. *arXiv preprint arXiv:2006.01981* (2020).
- [25] KINGMA, D., AND BA, J. Adam: A method for stochastic optimization. *arXiv preprint arXiv:1412.6980* (2014).
- [26] LEE, D.-H., ZHANG, S., FISCHER, A., AND BENGIO, Y. Difference target propagation. In *Joint European Conference on Machine Learning and Knowledge Discovery in Databases* (2015), Springer, pp. 498–515.
- [27] LILLICRAP, T. P., COWNDEN, D., TWEED, D. B., AND AKERMAN, C. J. Random feedback weights support learning in deep neural networks. *arXiv preprint arXiv:1411.0247* (2014).
- [28] LOTTER, W., KREIMAN, G., AND COX, D. Deep predictive coding networks for video prediction and unsupervised learning. *arXiv preprint arXiv:1605.08104* (2016).
- [29] MAASS, W. Networks of spiking neurons: the third generation of neural network models. *Neural networks* 10, 9 (1997), 1659–1671.
- [30] MINSKY, M. Steps toward artificial intelligence. *Proceedings of the IRE* 49, 1 (1961), 8–30.

- [31] MITTAL, S., LAMB, A., GOYAL, A., VOLETI, V., SHANAHAN, M., LAJOIE, G., MOZER, M., AND BENGIO, Y. Learning to combine top-down and bottom-up signals in recurrent neural networks with attention over modules. In *International Conference on Machine Learning* (2020), PMLR, pp. 6972–6986.
- [32] MOVELLAN, J. R. Contrastive hebbian learning in the continuous hopfield model. In *Connectionist Models*. Elsevier, 1991, pp. 10–17.
- [33] NØKLAND, A. Direct feedback alignment provides learning in deep neural networks. In *Advances in Neural Information Processing Systems* (2016), pp. 1037–1045.
- [34] OLSHAUSEN, B. A., AND FIELD, D. J. Sparse coding with an overcomplete basis set: A strategy employed by v1? *Vision research* 37, 23 (1997), 3311–3325.
- [35] OORD, A. V. D., LI, Y., AND VINYALS, O. Representation learning with contrastive predictive coding. *arXiv preprint arXiv:1807.03748* (2018).
- [36] ORORBIA, A. Spiking neural predictive coding for continual learning from data streams. *arXiv preprint arXiv:1908.08655* (2019).
- [37] ORORBIA, A., AND KIFER, D. The neural coding framework for learning generative models. *Nature communications* 13, 1 (2022), 1–14.
- [38] ORORBIA, A., MALI, A., GILES, C. L., AND KIFER, D. Continual learning of recurrent neural architectures by locally aligning distributed representations. *arXiv preprint arXiv:1810.07411* (2018).
- [39] ORORBIA, A., MALI, A., KIFER, D., AND GILES, C. L. Lifelong neural predictive coding: Sparsity yields less forgetting when learning cumulatively. *arXiv preprint arXiv:1905.10696* (2019).
- [40] ORORBIA, A., MALI, A., KIFER, D., AND GILES, C. L. Large-scale gradient-free deep learning with recursive local representation alignment. *arXiv e-prints* (2020), arXiv–2002.
- [41] ORORBIA, A. G., HAFFNER, P., REITTER, D., AND GILES, C. L. Learning to adapt by minimizing discrepancy. *arXiv preprint arXiv:1711.11542* (2017).
- [42] ORORBIA, A. G., AND MALI, A. Biologically motivated algorithms for propagating local target representations. In *Proceedings of the AAAI Conference on Artificial Intelligence* (2019), vol. 33, pp. 4651–4658.
- [43] ORORBIA, A. G., MALI, A., KIFER, D., AND GILES, C. L. Deep credit assignment by aligning local representations. *arXiv preprint arXiv:1803.01834* (2018).
- [44] PANICHELLO, M., CHEUNG, O., AND BAR, M. Predictive feedback and conscious visual experience. *Frontiers in Psychology* 3 (2013), 620.
- [45] RAINER, G., RAO, S. C., AND MILLER, E. K. Prospective coding for objects in primate prefrontal cortex. *Journal of Neuroscience* 19, 13 (1999), 5493–5505.
- [46] RAO, R. P., AND BALLARD, D. H. Dynamic model of visual recognition predicts neural response properties in the visual cortex. *Neural computation* 9, 4 (1997), 721–763.
- [47] RAO, R. P., AND BALLARD, D. H. Predictive coding in the visual cortex: a functional interpretation of some extra-classical receptive-field effects. *Nature neuroscience* 2, 1 (1999).
- [48] RAUSS, K., AND POURTOIS, G. What is bottom-up and what is top-down in predictive coding? *Frontiers in Psychology* 4 (2013), 276.
- [49] ROY, K., JAISWAL, A., AND PANDA, P. Towards spike-based machine intelligence with neuromorphic computing. *Nature* 575, 7784 (2019), 607–617.
- [50] RUMELHART, D. E., HINTON, G. E., AND WILLIAMS, R. J. Learning representations by back-propagating errors. *nature* 323, 6088 (1986), 533–536.
- [51] SALVATORI, T., SONG, Y., HONG, Y., SHA, L., FRIEDER, S., XU, Z., BOGACZ, R., AND LUKASIEWICZ, T. Associative memories via predictive coding. *Advances in Neural Information Processing Systems* 34 (2021), 3874–3886.
- [52] SALVATORI, T., SONG, Y., XU, Z., LUKASIEWICZ, T., BOGACZ, R., LIN, H., FAN, Y., ZHANG, J., BAI, B., XU, Z., ET AL. Reverse differentiation via predictive coding. In *Proceedings of the 36th AAAI Conference on Artificial Intelligence , AAAI 2022 , Vancouver, BC, Canada, February 22–March 1 , 2022* (2022), vol. 10177, AAAI Press, pp. 507–524.
- [53] SANTANA, E., EMIGH, M. S., ZEGERS, P., AND PRINCIPE, J. C. Exploiting spatio-temporal structure with recurrent winner-take-all networks. *IEEE Transactions on Neural Networks and Learning Systems* (2017).

- [54] SCELLIER, B., AND BENGIO, Y. Equilibrium propagation: Bridging the gap between energy-based models and backpropagation. *Frontiers in computational neuroscience* 11 (2017), 24.
- [55] SILVER, D., HUANG, A., MADDISON, C. J., GUEZ, A., SIFRE, L., VAN DEN DRIESSCHE, G., SCHRITTWIESER, J., ANTONOGLOU, I., PANNEERSHELVAM, V., LANCTOT, M., ET AL. Mastering the game of go with deep neural networks and tree search. *nature* 529, 7587 (2016), 484–489.
- [56] SONG, Z., ZHANG, J., SHI, G., AND LIU, J. Fast inference predictive coding: A novel model for constructing deep neural networks. *IEEE Transactions on Neural Networks and Learning Systems* 30, 4 (April 2019), 1150–1165.
- [57] SPRATLING, M. W. Predictive coding as a model of response properties in cortical area v1. *Journal of neuroscience* 30, 9 (2010), 3531–3543.
- [58] SPRATLING, M. W. A hierarchical predictive coding model of object recognition in natural images. *Cognitive computation* 9, 2 (2017), 151–167.
- [59] TIELEMAN, T., AND HINTON, G. Lecture 6.5—RmsProp: Divide the gradient by a running average of its recent magnitude. COURSE: Neural Networks for Machine Learning, 2012.
- [60] WEN, H., HAN, K., SHI, J., ZHANG, Y., CULURCIELLO, E., AND LIU, Z. Deep predictive coding network for object recognition. In *International Conference on Machine Learning* (2018), PMLR, pp. 5266–5275.
- [61] WHITTINGTON, J. C., AND BOGACZ, R. An approximation of the error backpropagation algorithm in a predictive coding network with local hebbian synaptic plasticity. *Neural computation* 29, 5 (2017), 1229–1262.

Appendix

In this appendix, we provide details on how to implement Conv-NGC in the form of residual block structures instead of the (de)convolutional form used in the main paper. Furthermore, Table 4 contains definitions of key acronyms/variables/operators used in the main paper.

6.1 Inference: Predicting and Correcting Neural Residual Blocks

State Block Prediction: Extending the prediction operation of Equation 1 to make use of stacks of operations, such as those that compose a residual block, is simple – the i th state feature map at ℓ , i.e., $\text{ReLU}(\mathbf{z}_i^\ell)$, is run through a series of convolution and pooling operations instead of just the single convolutional layer originally depicted in order to obtain a prediction of the i th state feature map at layer $\ell - 1$. For example, the residual block $R_s()$ we designed and employed in this paper entailed the following chain of operations:

$$\begin{aligned} \mathbf{h}_j^{\ell,4} &= \left(\sum_i^{C_\ell} \mathbf{W}_{ij}^{\ell,4} \odot_s \text{ReLU}(\mathbf{z}_i^\ell) \right) \\ \mathbf{h}_j^{\ell,3} &= \text{ReLU} \left(\text{Pool} \left(\sum_i^{C_\ell^4} \mathbf{W}_{ij}^{\ell,3} \odot_s \mathbf{h}_i^{\ell,4} \right) \right) \\ \mathbf{h}_j^{\ell,2} &= \text{Pool} \left(\sum_i^{C_\ell^3} \mathbf{W}_{ij}^{\ell,2} \odot_s \mathbf{h}_i^{\ell,3} \right) \\ \bar{\mathbf{z}}_j^{\ell-1} = \mathbf{h}_j^{\ell,1} &= \text{ReLU} \left(\sum_i^{C_\ell^2} \mathbf{W}_{ij}^{\ell,1} \odot_s \mathbf{h}_i^{\ell,2} \right) + \mathbf{z}_i^\ell \end{aligned} \quad (7)$$

where $\text{Pool}(\mathbf{v})$ denotes the max-pooling operation. Notice that $\mathbf{h}^{\ell,q}$ represents an “intermediate” layer within the ConvNCNet, or rather, an activity that exists within the residual block but does not count as an actual state. Specifically, s is the skip length of the residual block (in Equation 7 $s = 5$) and $\mathbf{h}_i^{\ell,q}$, where $q = \{s-1, s-2, \dots, 1\}$, which denotes the q th intermediate layer within the residual that relates \mathbf{z}_i^ℓ and $\mathbf{z}_i^{\ell-1}$. $\mathbf{W}_{ij}^{\ell,q}$ denotes the i th learnable filter associated with the q th intermediate layer calculation within the residual block. C_ℓ^q is the number of channels that make up an intermediate residual block layer \mathbf{h}_ℓ^q .

State Block Correction: State map correction in a residual blocks proceeds a bit differently from Equation 2 in the main paper, requiring further modification of the perturbation vector term \mathbf{d}_i^ℓ . Specifically, for the residual block we presented in Equation 7 above, this correction would become:

$$\mathbf{d}_i^\ell = -\mathbf{e}_i^\ell + \left(\sum_j^{C_\ell^3} \mathbf{E}_{ji}^{\ell,4} \mathbf{d}_j^{\ell,3} \right), \mathbf{d}_j^{\ell,3} = \sum_j^{C_\ell^2} \mathbf{E}_{ji}^{\ell,3} \mathbf{d}_j^{\ell,2}, \mathbf{d}_j^{\ell,2} = \sum_j^{C_\ell^1} \mathbf{E}_{ji}^{\ell,2} \mathbf{d}_j^{\ell,1}, \mathbf{d}_j^{\ell,1} = \sum_j^{C_{\ell-1}} \mathbf{E}_{ji}^{\ell,1} \mathbf{e}_j^{\ell-1} \quad (8)$$

where we observe that the learnable error synapses of the original LRA algorithm have been adapted to create a multi-step transmission pathway, i.e., a proxy teaching signal (instead of a layer-wise error neuron vector) is created for each intermediate layer, yielding a sort of hybrid between recursive LRA [40] and feedback alignment [27]. One could also view Equation 8 as one single error transmission pathway that is decomposed into a series of intermediate perturbation vectors (this view will be useful for crafting a fast update rule in the next sub-section). One key advantage of LRA is its flexibility in designing information transmission pathways that do not necessarily need to strictly mirror the flow of the forward transmission pathway [40]. In Equation 8, this flexibility comes into play given that the error transmission pathway skips over non-learnable operations such as pooling and activation functions, quickly facilitating the calculation of the perturbation needed to correct feature map state \mathbf{z}_i^ℓ .

6.2 Training: Updating Model Parameters

Residual Block Update: To train the residual block synapses, we would adapted the LRA algorithm to train the intermediate transformations within the block. Specifically, we take further advantage of the multi-step error transmission pathway presented in Equation 8 to craft a simple update rule (specifically, using recursive-LRA [40] offers the greatest amount of flexibility in the design of error transmission pathways). As a result, the rule for

Table 4: Table of key symbol/operator/abbreviation definitions.

Item	Explanation
Conv-NGC	Convolution neural generative coding (model)
$*_s$	strided convolution where s is the stride argument
\oslash_s	denotes deconvolution (or transposed convolution) with a stride of s
\cdot	Matrix/vector multiplication
\odot	Hadamard product (element-wise multiplication)
$()^T$	denotes the transpose operation
Flatten(\mathbf{z})	input tensor \mathbf{z} is converted to a column vector
UnFlatten(\mathbf{z})	is inverse of Flatten(\mathbf{z})
Dilate(\mathbf{v}, s)	represents a dilation function controlled by the dilation (integer) size s
\mathbf{W}_{ijkl}	represents a 4-dimensional tensor or synaptic weights
\mathbf{E}_{ijkl}	represents a 4-dimensional tensor or synaptic error weights
\bar{L}	denotes set of predictive layers
\mathbf{z}^ℓ	denotes state representation at layer ℓ
$\bar{\mathbf{z}}^{\ell-1}$	denotes state prediction at layer ℓ
$\mathbf{e}^{\ell-1}$	denotes the error/mismatch signal at layer $\ell - 1$
$\phi^\ell()$	denotes the activation/transfer nonlinear activation applied to the state tensor
$g^\ell()$	denotes the activation/transfer nonlinear activation applied to the state tensor prediction
\leftarrow	denotes a variable override and the modulation/adjustment factor
β	denotes constant value, which controls the state correction rate
γ	denotes the strength factor to control leak variable
T	Total number of iterations for iterative inference in Conv-NGC
λ	denotes the modulation factor to control the evolution of the error filters

adapting the parameters of a residual block is:

$$\Delta \mathbf{W}_{ij}^{\ell,q} = \mathbf{d}_j^{\ell,q-1} *_1 \text{Dilate}\left(\left(\phi^\ell(\mathbf{h}_i^{\ell,q})\right)^T, s\right), \quad \Delta \mathbf{E}_{ji}^\ell = \lambda \left((\Delta \mathbf{W}_{ij}^{\ell,q})^T \right), \quad (9)$$

where $\mathbf{d}_j^{\ell,0} = \mathbf{e}_j^{\ell-1}$, and $\mathbf{h}_i^{\ell,s} = \mathbf{z}_i^\ell$.

The key difference between the neural coding and residual block updates is the use of $\mathbf{d}_i^{\ell,q}$ for the weight/filter update. As shown in Equation 8, $\mathbf{d}_i^{\ell,q}$ is computed using errors from the layer below it and simply represents a perturbation that could be applied to its respective layer/transformation to help it better predict the downstream target $\mathbf{z}_i^{\ell-1}$. In effect, this rule functions similar in spirit to backprop in that it directly provides a (proxy) teaching signal that only affects the weights but not the activities of the neurons of a given layer. We found this to be a fast and effective rule for updating the parameters of blocks that contained stacks of operations of length greater than one, i.e., residual blocks, in order to achieve performance comparable to ResNet trained with backprop. (Note that one could, instead, utilize backprop to compute the local gradients/adjustments of the intermediate filters/activities of the block instead, offering an even more stable update scheme for within a block.)